Volume 28
Number 15
22 April 2026
Pages 8997–9814

PCCP

Physical Chemistry Chemical Physics

rsc.li/pccp

ISSN 1463-9076

ROYAL SOCIETY OF CHEMISTRY

PAPER
Adolfo B. Poma *et al.*
A comparative nanomechanical study of antibody and nanobody binding to SARS-CoV-2 variants

PCCP Owner Societies

PCCP

ROYAL SOCIETY OF CHEMISTRY

PAPER

View Article Online
View Journal | View Issue

Cite this: *Phys. Chem. Chem. Phys.*, 2026, **28**, 9159

A comparative nanomechanical study of antibody and nanobody binding to SARS-CoV-2 variants

Luis F. Cofas-Vargas, *[a] Gustavo E. Olivos-Ramirez, [b] Siewert J. Marrink [c] and Adolfo B. Poma *[b]

The receptor-binding domain (RBD) of the SARS-CoV-2 spike protein is the main target of neutralizing antibodies (Abs) and nanobodies (Nbs). Although their binding affinities are well characterized, their mechanical stability under force remains poorly understood, despite its relevance in viral attachment, immune recognition, and receptor engagement. Here, we present a comparative nanomechanical analysis of three Abs (PDI-231, S2X259, and R1-32) and three Nbs (R14, C1, and *n*3113.1) bound to the RBD from the WT and Omicron variants BA.4 and JN.1. Using steered molecular dynamics within the Martini 3 coarse-grained framework, we identified distinct mechanical signatures determined by epitope topology, binding architecture, and variant-specific mutations. Ab/RBD complexes display asymmetric rupture events in which the heavy chain serves as the main pathway for force transmission, while the light chain provides secondary reinforcement. The cooperative action of both chains enhances mechanical resilience, supporting rupture forces near 500 pN. In contrast, Nb/RBD complexes exhibit rigid-body dissociation with direct force transmission through compact single-domain scaffolds and minimal structural deformation. Variant-dependent unfolding of RBD regions, particularly residues 438–507 and 516–529, appears as a recurrent fracture motif contributing to adaptive mechanical response. These results establish mechanical stability as a key descriptor of immune complex robustness, complementing thermodynamic affinity. By linking architecture, epitope geometry, and force propagation, this study provides a quantitative framework for designing antibodies and nanobodies with improved mechanical resilience against viral evolution.

Received 14th February 2026,
Accepted 27th February 2026

DOI: 10.1039/d6cp00556j

rsc.li/pccp

1. Introduction

The coronavirus disease (COVID-19) pandemic, caused by the betacoronavirus severe acute respiratory coronavirus 2 (SARS-CoV-2), has resulted in millions of infections and deaths worldwide.[1] SARS-CoV-2 encodes four structural proteins, including the trimeric spike (S) glycoprotein, which facilitates virus entry through recognition of the human angiotensin-converting enzyme 2 (hACE2).[2] Each S monomer is composed of an N-terminal S1, responsible for receptor binding, and a C-terminal S2 subunit, which drives membrane fusion.[3] Within S1, the receptor-binding domain (RBD; residue range R319-F541) sits at the apex of the trimer and contains the receptor-binding motif (RBM) comprising residues S438-Q506, which directly engages hACE2.[4,5]

The RBD is a primary target of human neutralizing antibodies (Abs) and engineered nanobodies (Nbs) because of its crucial role in host recognition.[6] Mutations within the RBM have been key drivers in the emergence of SARS-CoV-2 variants of concern (VOCs), leading to increased transmissibility and immune evasion.[7,8] For example, the N501Y mutation, present in the Alpha and Omicron variants, enhances the binding affinity to hACE2, while the E484K and L452R, found in Beta, Gamma, and Delta, reduce the neutralization efficiency of therapeutic Abs.[9] These mutations pose a persistent threat to the clinical efficacy of current therapeutic treatments.

Beyond its clinical relevance, the SARS-CoV-2 RBD provides an ideal model system for method development in protein–protein interaction studies. The RBD/hACE2 interaction is one of the most extensively characterized interfaces in structural biology, with dozens of high-resolution structures resolved by X-ray crystallography and cryo-electron microscopy, covering multiple viral lineages and conformational states.[10–12]

Because viral entry begins with this molecular recognition step, the biophysical properties of the RBD/hACE2 interaction under mechanical stress are key to understanding infectivity and immune escape. Traditional affinity and neutralization

[a] *Departamento de Química, Universidad Autónoma Metropolitana-Iztapalapa, Ciudad de México, Mexico. E-mail: fcofas@xanum.uam.mx*
[b] *Biosystems and Soft Matter Division, Institute of Fundamental Technological Research, Polish Academy of Sciences, ul. Pawińskiego 5B, Warsaw 02-106, Poland. E-mail: apoma@ippt.pan.pl*
[c] *Groningen Biomolecular Sciences and Biotechnology Institute, University of Groningen, Nijenborgh 7, 9747 AG Groningen, The Netherlands*

data provide thermodynamic insights but do not fully capture the mechanical properties, which may be relevant in physiological and therapeutic contexts.[13] During infection, forces such as fluid shear stress, tissue deformation, and intracellular crowding act on viral and host components.[14] Therefore, the mechanical stability of the RBD in complex with hACE2 or neutralizing agents has direct implications for viral attachment, immune evasion, and therapeutic resistance.

Recent studies using single-molecule force spectroscopy (SMFS) and molecular dynamics (MD) simulations have shown that the mechanical stability of RBD/hACE2 complexes varies across SARS-CoV-2 variants.[7] Notably, variants such as Alpha, Beta, and Omicron exhibit increased force resistance at the RBD/hACE2 interface, consistent with enhanced binding affinity and transmissibility. However, while the nanomechanics of hACE2 complexes have been extensively studied, the nanomechanical properties of SARS-CoV-2 RBD binding neutralizing Abs and Nbs remain largely unexplored.[15–18]

Abs and Nbs differ in their size, structure, and binding mechanisms. Conventional Abs are bivalent ~150 kDa molecules composed of heavy (H) and light (L) chains, while Nbs are an order of magnitude smaller single-domain proteins derived from camelid heavy-chain-only Abs.[19,20] These structural differences influence not only epitope accessibility but also the distribution and transmission of mechanical forces during complex dissociation. Understanding how these biomolecules behave under force is essential for designing more robust therapeutics. Particularly, Nbs have attracted attention for their favorable biophysical properties, including high solubility, thermal stability, and the ability to bind cryptic epitopes on viral proteins.[20] Several Nbs have shown potent neutralization against SARS-CoV-2. Among these, the llama-derived Nb H11-H4 binds a conserved epitope on the RBD with nanomolar affinity and has been shown to block viral entry *in vitro*.[21]

Although SMFS provides valuable insights into rupture forces of Abs or Nb-antigen complexes,[7,22] it cannot fully resolve the molecular determinants governing these events. Protein complexes experience mechanical stress *in vivo* due to respiratory flow, receptor-mediated endocytosis, blood flow, *etc.*[14,23] Such forces can induce partial unbinding and select for mechanically resilient binders, influencing neutralization efficacy.[7,24] SMD thus provides a controlled framework to mimic these tensile conditions and quantify the intrinsic stability of antibody and nanobody interfaces under load. To address these limitations, we employed the GōMartini 3,[25] a methodology that combines the Martini 3 force field[26] with a structure-based model.[27] In this framework, contacts are defined based on an optimised protein contact map that considers the overlap (OV) of the van der Waals radii and the repulsive contacts of structural units (rCSU) between heavy atoms.[28] GōMartini 3 enables accurate mechanical characterization of large biomolecular complexes at reduced computational cost while allowing for slower and more realistic pulling velocities.[15,25] Unlike traditional CG models that rely on harmonic restraints, GōMartini 3 preserves the tertiary and quaternary structures of proteins and permits large-scale conformational changes.[25]

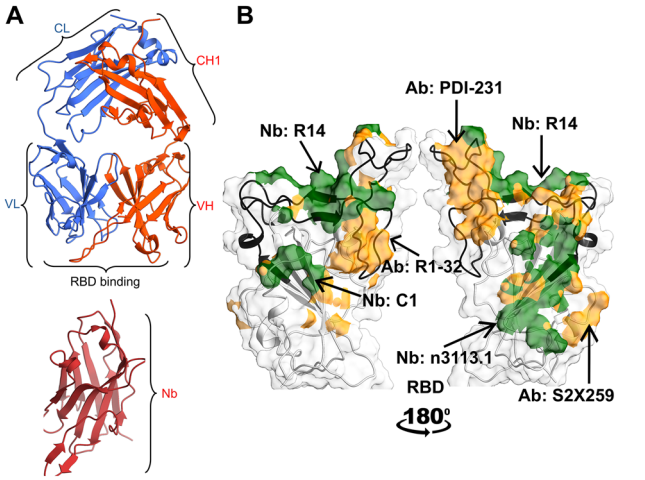

Fig. 1 Structural overview of Ab and Nb recognition of the SARS-CoV-2 RBD. (A) Domain organization of a conventional Ab (top) comprising the L chain (variable region (VL), and constant region (CL), shown in blue) and the H chain (variable region (VH), and first constant domain (CH1), shown in orange), and the bottom shows the single-domain variable region of a heavy-chain-only Ab (Nb, shown in red). (B) Representative binding footprints of Abs (PDI-231, R1-32, S2X259) and Nbs (R14, C1, *n*3113.1) on the RBD (cartoon in black, surface representation in gray). Epitope regions targeted by each Ab and Nb are highlighted on the RBD surface in orange and green. The two panels show the RBD rotated by 180° to visualize binding epitopes from opposite orientations. The RBM region is highlighted in black color.

In this study, we performed a comparative nanomechanical analysis of six RBD complexes comprising three Abs and three Nbs, each binding a distinct region of the RBD (Fig. 1). We selected systems with available experimental structures and modeled two SARS-CoV-2 Omicron variants, BA.4 and JN.1, to assess the effects of mutations on mechanical behavior. Each complex was first relaxed using AA-MD simulations and then subjected to CG-SMD simulations using GōMartini 3. In addition to intact Abs, we designed single-chain systems in which either the H or L chain was bound alone to the RBD, enabling us to probe the individual contributions of each chain to force transmission. By analyzing the rupture of contacts under force, we compared the nanomechanical resilience of Ab- and Nb-bound RBD complexes, and dissected how cooperative *versus* individual chain contributions shape their response. Our findings reveal how structural architecture and binding orientation govern the nanomechanical stability of these immune complexes, offering insights for the rational design of therapeutics with enhanced mechanical robustness.

2. Methods

2.1. Molecular modeling

We first generated complete structural models of Ab and Nb complexes with the SARS-CoV-2 RBD, which served as an input for subsequent relaxation and nanomechanical analysis. Six representative complexes were selected to cover distinct epitopic regions of the RBD.[29] These included three Abs, PDI-231 (PDB ID: 7MZN; class 1A),[30] S2X259 (PDB ID: 7M7W; class 4A),[31] and

Table 1 Structural and binding parameters of the selected Abs targeting the SARS-CoV-2 RBD. For each protein case, the name, type, PDB ID, and RBD residues making contacts with the WT are listed. Experimental dissociation constant (K_D) parameters considering different variants are reported. Residues in bold are part of the RBM region[30,32,58,59]

Ab	PDI-231 (PDB ID: 7MZN)			S2X259 (PDB ID: 7M7W)			R1-32 (PDB ID: 7YDI)		
Variant	WT	BA.4	JN.1	WT	BA.4	JN.1	WT	BA.4	JN.1
RBD binding residues	T415	*	*	Y369	-	-	G325	-	-
	K417	N417	N417	N370	-	-	A326	-	-
	D420	*	*	S371	-	-	Y328	-	-
	R457	*	*	A372	*	*	R346	*	-
	K458	*	*	F374	*	*	S390	*	-
	S459	*	*	S375	F375	F375	S393	*	-
	N460	*	*	T376	-	-	**K462**	-	*
	Q474	*	*	F377	*	*	**P463**	-	*
	A475	*	*	K378	*	*	**E465**	-	*
	G476	*	*	C379	*	*	**R466**	*	*
	E484	-	-	Y380	*	*	**D467**	*	*
	G485	*	*	V382	*	*	**I468**	*	*
	N487	*	*	S383	*	*	**S469**	*	*
	C488	*	*	P384	*	*	**T470**	-	*
	Y489	*	*	T385	*	*	**E471**	*	*
	-	-	E493	D405	-	-	**F490**	*	-
	Y421	*	*	R408	-	-			
	G502	*	*	**G502**	*	-			
	Y505	**H505**	**H505**	**V503**	*	*			
				G504	*	-			
				Q506	*	-			
K_D app. (nM)	0.38^{a++30}			$<0.1^{a+58}$ 52.6^{d+59}			0.8^{a++32} 0.71^{b++32} 10^{c++32}		

[a]WT [d]Omicron BA.4/5 [†]Surface plasmon resonance (SPR)
[b]Alpha *Same contact [††]Bio-layer interferometry (BLI)
[c]Beta -Missing contact

R1-32 (PDB ID: 7YDI; class 4B),[32] and three Nbs, R14 (PDB ID: 7WD1; class 2A),[33] C1 (PDB ID: 7OAP; class 3A),[34] and *n*3113.1 (PDB ID: 7VNE; class 5B).[35] Together, these systems span all major RBD topological zones, from ACE2-competitive epitopes to cryptic and conserved regions associated with cross-variant recognition.[29] Missing residues in 7M7W (residues 141–147) were modeled using Modeller v10.5.[36] In the 7YDI structure, hACE2 was removed, while for 7VNE, only the RBD/Nb portion was retained. To avoid artificial termini charges, the N- and C-termini of the RBD, H and L chains, and Nb (where needed) were capped with acetyl and methylamide groups, respectively. Additionally, BA.4 and JN.1 SARS-CoV-2 Omicron variants were modeled using the WT RBD as a template, incorporating the corresponding mutations *via* Modeller while preserving the original Ab or Nb binding geometry. Table 1 summarizes the structural and binding features of Ab and Nb targeting the WT RBD. A full list of protein contacts for all complexes is provided in Tables S2–S7.

2.2. AA-MD simulations

AA-MD simulations were then performed to relax each complex and to obtain equilibrated structures suitable for CG modeling within the GōMartini 3 framework. These simulations were carried out using the AMBER 24 software package with the ff19SB force field.[37,38] Simulations were run with the GPU-accelerated pmemd.cuda engine.[39] Initial energy minimization in a vacuum was performed for each complex to eliminate steric clashes, particularly around mutated residues introduced during modeling. The protonation state of titratable residues was assigned at pH 7.4 using PDBFixer.[40]

Each minimized complex was solvated in a dodecahedral box of explicit water molecules using the four-site OPC water model,[41] with a minimum distance of 10 Å between any protein atom and the box edge. System neutrality was achieved by adding Cl- counterions, with the number of ions adjusted based on the net charge of each system. The number of ions added ranged from 2 to 12, depending on the SARS-CoV-2 variant (*i.e.*, WT, BA.4, and JN.1).

Following solvation, systems underwent 5000 steps of energy minimization using the steepest descent algorithm to resolve unfavorable contacts and to allow for solvent relaxation. Temperature equilibration was performed under constant volume (NVT) conditions by incrementally increasing the temperature from 150 K to 310 K in five 200-ps steps. During this phase, harmonic position restraints were applied to protein heavy atoms, with spring constants progressively reduced from 5 to 1 kcal mol^{-1} $Å^{-2}$ to permit gradual relaxation of the protein backbone and side chains. This was followed by a 1 ns unrestrained equilibration at 310 K under constant pressure (NPT) conditions.

Production simulations were conducted in the NPT ensemble using periodic boundary conditions. Long-range electrostatics were treated with the particle mesh Ewald method, employing a grid spacing of 1 Å. Short-range interactions were modeled using a Lennard-Jones (LJ) potential with a 9 Å cutoff.[42,43] Temperature was regulated using Langevin dynamics with a collision frequency of 4 ps^{-1},[44] while pressure was maintained at 1 bar using the Monte Carlo barostat with a relaxation time of 2 ps.[45] Covalent bonds involving hydrogen atoms were constrained using the SHAKE algorithm,[46] and hydrogen mass repartitioning was applied using ParmEd,[47] allowing the use of a 4 fs integration time step.[48] Each system was simulated for 500 ns. All complexes remained structurally stable throughout the simulations.

2.3. Contact map determination

To identify high-frequency contacts (Olivos-Ramirez *et al.* 2025) at the interface of each complex from AA-MD simulations, we analyzed the atomistic MD trajectories of Ab or Nb/RBD systems. Each system was simulated for 500 nanoseconds, and contacts were calculated every 1 nanosecond using a Python script (https://github.com/GoMartini3-tools/ContactFreq). This script uses the executable version of the Go Contact Map from the server (https://pomalab.ippt.pan.pl/GoContactMap/) which is also available at https://zenodo.org/records/3817447 and https://github.com/Martini-Force-Field-Initiative/GoMartini/tree/main/ContactMapGenerator.

We considered both the van der Waals (vdW) radii overlap (OV) and repulsive chemical structural units (rCSU) contact map methods.[28,49] The OV contact map method is a purely geometric criterion that identifies interactions based on the spatial overlap of vdW spheres centered on heavy atoms. To incorporate attractive contributions, each vdW radius is scaled by a factor of 1.24. A contact is defined when spheres from two residues, separated by at least four positions in the sequence, overlap. This approach has been widely used to identify stabilizing interactions relevant for folding and mechanical unfolding of protein domains.[15,27,49–51] The rCSU method complements the OV approach by integrating chemical specificity and electrostatics. It considers both attractive and repulsive interactions and classifies residues as hydrophobic, hydrophilic, aromatic, or ionic. A contact is considered valid when the number of attractive interactions exceeds the number of repulsive ones. Each atom is represented as a sphere, and its surface is sampled using a Fibonacci grid, which ensures a uniform and unbiased distribution of points. Only high-frequency contacts, defined as those present in more than 70 percent of the frames, were retained. The frame containing the largest number of contacts was selected for CG modeling using the GōMartini 3 framework (Tables S2–S7).

2.4. CG-MD simulations

CG models for Ab and Nb complexes were prepared using the Martini 3 force field[26] and the martinize2 tool.[52] Secondary structure definitions were assigned using DSSP v3.0.[53] We applied the GōMartini 3 approach,[25,27] which incorporates a Lennard-Jones potential between virtual sites derived from the high-frequency contact map.[54] The depth of the LJ potential for contact pairs was set to 15 kJ mol^{-1}.[15,51] The CG structures were initially minimized in a vacuum during 5000 steps using the steepest descent algorithm. Subsequently, the complexes were solvated in a $2 \times 2 \times 2$ nm^3 box with the standard Martini water model. Sodium and chloride ions were added to neutralize each system and to achieve a physiological strength of 0.15 M.

Positional restraints were imposed on the BB beads of each protein to prevent drifting during the equilibration phases. Both the NVT and NPT equilibrations, along with the production phase, utilized the V-rescale thermostat.[55] The temperature coupling time constant was set at 1.0 ps for both protein and solvent components of the system, keeping the temperature at 300 K. The NVT equilibration was run for 2 ns, with an integration time of 20 fs. During the NPT equilibration and production, an isotropic pressure coupling was used with a compressibility set at 10^{-4} bar^{-1} and 1 bar pressure. The NPT equilibration was run for 5 ns using the C-rescale barostat[56] with a pressure coupling time constant of 12 ps and an integration time of 10 fs. For the production phase, the C-rescale barostat was used, with a pressure coupling time constant of 15 ps. The cutoff distances for Coulomb and van der Waals (vdW) interactions were set at 1.2 nm across all equilibration and production phases. The equilibrium simulations were conducted over 2 microseconds, with a time step of 20 fs. A total of 5 independent replicas were conducted for each system using GROMACS 2023.5.[57]

We monitored interfacial contact frequency over 2 μs equilibrium simulations (Fig. S16–S19). All RBD/Ab and RBD/Nb complexes preserved their characteristic binding interfaces, with contacts maintained with high frequency throughout the trajectories. While some variant-specific contacts showed moderate fluctuations, the dominant interaction networks remained stable across replicas. These results indicate that the GōMartini parametrization reliably sustains the binding modes of the complexes under equilibrium conditions, providing robust starting points for the nanomechanical pulling simulations.

2.5. CG-SMD simulations

Systems were prepared as stated in the previous subsection. All CG systems were initially energy-minimized in vacuum for 5000 steps using the steepest descent algorithm. To accommodate the pulling geometry, complexes with conventional Abs were solvated in a $10 \times 10 \times 100$ nm^3 water box, and RBD/Nb complexes in a $10 \times 10 \times 80$ nm^3 box. Minimization and equilibration cycles matched those described above. Production runs used the same barostat with a 8 ps coupling time and a 20 fs integration time step. The cutoff for both Coulombic and van der Waals interactions was set to 1.2 nm throughout all stages.

SMD simulations were carried out for 2.5–3.0 μs per replica. Directional constraints were applied to mimic mechanical dissociation. The heavy atoms of the last three residues at the RBD C-terminus were restrained along the pulling axis (z), while the last three residues of the Nb or the Ab H or L chain were fixed in the x- and y. The pulling force was applied to the center of mass of the selected terminus using a constant velocity of 1×10^{-5} nm ps^{-1} and a harmonic spring constant of 37.6 kJ mol^{-1} nm^{-2}. For conventional Abs, two separate pulling sets were defined: (i) pulling from the H chain, and (ii) pulling from the L chain. A total of 50 independent replicas were performed for each configuration using GROMACS 2023.5.[57]

Single-chain antibody systems were derived from the same equilibrated starting structures used for the full complexes by deleting either the H or the L chain before system preparation (see above). All other settings were identical to the full-complex protocol. These reduced systems enabled us to isolate and evaluate the individual contributions of each chain to the overall mechanical response.

To evaluate the dynamic stability of protein–protein interfaces during CG pulling simulations, we systematically monitored the rupture of contacts throughout each trajectory. The analysis was based on an effective representation of atoms as enlarged vdW spheres, which better approximate the spatial extent of atoms by accounting for the influence of their electron clouds. Contact pairs were defined according to the interaction list specified in the GōMartini framework. For each contact, a specific σ value was assigned, corresponding to the distance at which the LJ potential equals zero. The position of the potential energy minimum (R_{min}) was then calculated as σ multiplied by $2^{\frac{1}{6}}$. During the simulations, we computed the distance between the BB beads of each contact pair at every frame and compared it to a scaled threshold, set to 1.3 times R_{min}, following previous GōMartini studies.[15] A contact was considered intact if the BB–BB distance was less than or equal to this threshold; otherwise, it was classified as broken.

3. Results & discussion

3.1. Molecular basis of Ab–RBD interactions

To investigate the determinants of stability in the RBD/PDI-231 complexes, we analyzed the interfacial contacts across SARS-CoV-2 RBD variants. The H chain comprises a variable domain (VH, residues 1–124) and a constant domain (CH1, residues 133–228), while the L chain consists of a variable domain (VL, residues 1–112) and a constant domain (CL, residues 121–217).[30] The interface is mainly formed by VH and CH1 from the H chain and the VL domain from the L chain. A persistent network of hydrophobic, polar, and aromatic interactions stabilizes the complex K378 from the RBD interacting with Y102, Y103, and W105 from VH through cation–π interactions, and Y380 forming hydrophobic contacts with N101 and Y102. CH1 contributes polar contacts with RBD residues D405 and G502 *via* CL residues. A conserved RBD segment (residues 515–529) engages both VH and VL, creating a hydrophobic core (F490, Y489, and A475) that persists in BA.4 and JN.1. In contrast, ionic interactions such as K458–E50 and R457–D52 observed in the WT complex are lost in Omicron variants due to mutations such as K417N and E484A. Despite these changes, CL-mediated interactions (*e.g.*, Y103 and Y52 with Y421 and G485) remain conserved, highlighting the stabilizing role of the L chain (Table S2).

Analysis of the WT/S2X259 complex revealed a predominantly hydrophobic interface centered on VH residues (residues 1–124), where A375, C379, S375, and F377 form frequent contacts with RBD residues Y505, F456, and G476. These interactions are localized within the complementarity-determining regions (CDRs), particularly CDR1_H (residues 25–33), CDR2_H (residues 52–58), and CDR3_H (residues

100–112), forming a compact, structurally resilient hydrophobic core.[31] In contrast to PDI-231, S2X259 establishes few ionic interactions; the K378–Y505 and K378–G476 pairs observed in the WT complex are lost in the BA.4 and JN.1, reducing electrostatic complementarity. Nonetheless, the BA.4 preserves key hydrophobic interactions such as S375–Y505 and C379–F456, maintaining an overall similar interface. In JN.1, interfacial contacts decrease substantially, especially those involving the CL domain (residues 121–217), which are fully lost. Despite this reduction, conserved interactions between VH and RBD (A375–Y505 and F377–F456) maintain partial interfacial stability. These observations indicate that S2X259 primarily relies on VH-mediated hydrophobic contacts for RBD recognition, with minimal contribution from CL in the Omicron variants (Table 1 and Table S2).

The H chain of R1-32 comprises a VH domain (residues 1–122) and a CH1 domain (residues 131–228), while the L chain contains a VL domain (residues 1–110) and a CL domain (residues 119–214).[32] In the WT complex, binding is dominated by VH-mediated hydrophobic contacts within CDR1 and CDR2 (E484–Y102, F486–Y52, F486–Y103, and Y489–Y52), forming a stable hydrophobic core reinforced by polar interactions such as D467–Y102 and E465–Y105. The CH1 domain contributes marginally through residues S409 and T470. In BA.4 and JN.1, these key VH contacts are preserved, but multiple CH1- and CL-mediated interactions (S409, T470, S390) are lost, reducing peripheral stabilization. The L chain contributes fewer contacts overall, with S390–K528 unique to WT. Variant-specific electrostatic interactions, including K356–S391 and N354–S391 in BA.4, and N354–S391 in JN.1, appear to compensate partially for the loss of hydrophobic contacts. Overall, R1-32 maintains binding primarily through conserved VH hydrophobic contacts, while Omicron mutations remodel secondary interactions at CH1 and CL.

3.2. Molecular basis of Nb–RBD interactions

R14 engages the RBM through a compact interface dominated by hydrophobic and aromatic contacts, mainly involving F490 of the RBD, which contacts Y104, Y109, and T102 of the Nb and Y449, which interacts with A101, Y103, and Y31 of the Nb.[33] Polar stabilization is provided by the Q493–T102 contact. In the WT complex, F486 contributes multiple hydrophobic interactions that are lost in BA.4 and JN.1, reducing interfacial packing. JN.1 exhibits the lowest number of total contacts, consistent with a more disrupted interface. Compared with PDI-231, which exhibits a mixed network of hydrophobic, polar, and ionic interactions such as K458–E50 and R457–D52 in WT, R14 relies primarily on a localized hydrophobic and aromatic core. This contact profile likely explains its reduced affinity for Omicron BA.4 (K_D = 43.3 nM) relative to WT, where no dissociation was detected.

The C1 binding surface partially overlaps the S2X259 epitope.[34] In the WT complex, recurrent interactions include K378–A102/D105/F101/G103, F377–G103, G381–F31, and hydrophobic pairs Y380–F101 and V382–F31. These are supported by a polar cluster involving S383 (with S54 and T106) and R408–S109. Most contacts are preserved in BA.4, which also introduces new ionic pairs such as K378–D105 and K378–R104. In

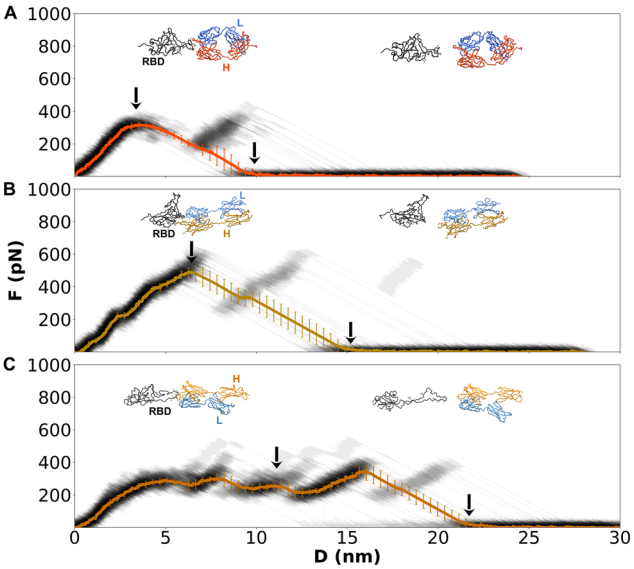

Fig. 2 Mechanical response of Ab/RBD WT complexes under constant-velocity pulling from the H chain. Force–displacement profiles are shown for (A) PDI-231, (B) S2X259, and (C) R1-32 (gray traces, mean in color). Insets display representative structures at the maximum force (F_{max}, left arrow) and after dissociation (right arrow). Error bars denote standard deviations across 50 independent trajectories.

JN.1, the interface remains centered on hydrophobic anchors Y380–F101 and V382–F31. Compared with S2X259, whose hydrophobic core involves F486, Y489, and A475, C1 maintains its key hydrophobic interactions across variants and compensates for the loss of polar or ionic contacts by reorganizing interactions around K378.

*n*3113.1 forms a compact interface centered on a hydrophobic pocket where A348 and A352 of the RBD contact A100 of the Nb, together with I468–Y32 and the conserved Y449–W47 pair.[35] These interactions are complemented by a polar network involving R346–D106 and residues around N354 and T345, whose specific pairs vary between variants. In WT, N354–S101 and T345–S103 are observed, whereas BA.4 retains T345–S103 but loses N354 contacts. In JN.1, N354 interacts with S101 or T104, and a new T356–T104 contact appears. The number of total contacts decreases in BA.4 (n = 17) but partially recovers in JN.1 (n = 23) due to new polar contacts such as N354–S101/T104 and T356–T104 and D450–W47. Compared with R-32, which features a broader interface dominated by VH contacts to E484, F486, and Y489 with additional CH1 and CL contributions, *n*3113.1 maintains a smaller but cohesive hydrophobic core that persists across variants.

Overall, the Abs and Nbs examined displayed distinct strategies for RBD recognition, ranging from broad, mixed hydrophobic–polar interfaces (PDI-231, R1-32) to more localized hydrophobic/aromatic cores (R14, C1, *n*3113.1). Omicron BA.4 and JN.1 disrupt several ionic and peripheral contacts, particularly in constant-domain and light-chain regions, while core VH or Nb–RBD hydrophobic contacts are generally preserved. R14 and S2X259 showed marked contact loss in JN.1, consistent with reduced affinity, whereas C1 and *n*3113.1 compensate through alternative polar or

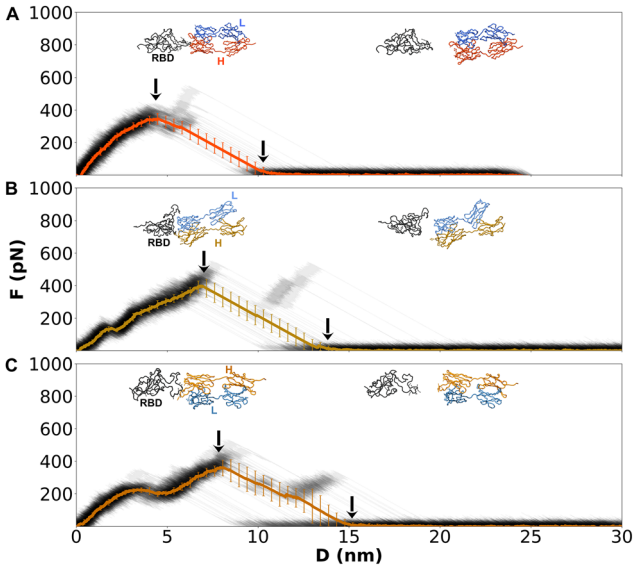

Fig. 3 Mechanical response of Ab/RBD JN.1 complexes under constant-velocity pulling from the H chain. Force–displacement profiles are shown for (A) PDI-231, (B) S2X259, and (C) R1-32 (gray traces, mean in color). Insets display representative structures at the maximum force (F_{max}, left arrow) and after dissociation (right arrow).

ionic interactions. These patterns highlight both the vulnerability of certain epitopes to variant mutations and the capacity of others to adapt *via* contact reorganization.

3.3. Nanomechanics of Ab/RBD complexes

The binding affinity of Abs has been extensively characterized.[60] More recently, we demonstrate the inherent mechanical stability present in potent neutralizing Nbs across different SARS-CoV-2 variants,[15] but the relative contribution of the H and L chains to mechanical stability remains poorly understood. To address this gap, we employed SMD simulations to probe the Ab response under force by applying constant-velocity pulling either from the C-terminus of the H chain or from the L chain in independent simulations. This setup allowed us to monitor force-displacement profiles, identify dissociation pathways, and assess the stabilizing role of inter-chain contacts during mechanical stress.

3.3.1. PDI-231/RBD complex. Both PDI-231 and R14 are hACE2-competing binders that neutralize SARS-CoV-2 by blocking spike-receptor recognition. PDI-231 is a monoclonal Ab that binds directly to the RBM of the RBD, overlapping with the hACE2 binding site.[30] It exhibits high affinity for the WT variant (K_D = 0.38 nM) and retains neutralizing activity against multiple variants, including those carrying N501Y, E484K, and K417N.[30] Due to its epitope location, PDI-231 can bind only to the RBD in the up conformation.[30] Mechanical dissociation was first analyzed for the WT complex using 50 independent CG-SMD simulations (Fig. 2A). Pulling the H chain produced two distinct dissociation behaviors. In most trajectories, the force–displacement profile displayed a single major peak (Fig. 2A), indicating rigid-body dissociation where both Ab chains (H in red and L in blue) and the RBD (black) remained folded from the point of maximum force until full dissociation. In approximately 28% of trajectories, partial unfolding of the H chain C-terminal region (residues V207–D226) preceded dissociation, while the RBD retained its structural integrity (Fig. S1A). Across all CG-SMD trajectories, the H chain was consistently the last component to dissociate.

When SMD pulling was applied to the L chain (Fig. S5A), dissociation also followed a rigid-body mechanism. In this case, unfolding of RBD residues A522–H530 was frequently observed (Fig. S1B), reflecting the weaker load-bearing capacity of the L chain. The H chain absorbed most of the force, reducing deformation of the RBD, whereas L-chain pulling transmitted stress more directly, promoting local unfolding (A522–H530 segment).

Analysis of inter-chain contacts of PDI-231 in the WT complex (Fig. S12 and Table S2) revealed that S114-S141, located in the constant domains, was the first contact to rupture under force. Additional CH1-CL pairs such as F118-L133, T164-F175, S162-P176, and V163-P176 also ruptured early, indicating that the CH1-CL interface detaches readily regardless of the pulled chain.

For the BA.4 variant, pulling from either chain led predominantly to rigid-body dissociation. The L chain consistently detached before the H chain (Fig. S2A, S6A and S8A). Limited unfolding of the H-chain C-terminal residues (I204–D226, K215-D226) was occasionally observed prior to rupture. Pulling from the L chain again yielded rigid-body separation, with rare unfolding events in the L-chain C-terminal region (residues E195–C214) in 4% of the trajectories (Fig. S2C). Compared with WT, seven inter-chain contacts in CH1 and CL (T192-N137, V178-Q160, P176-S162, P176-V163, F175-S162, F175-V163, F175-T164) exhibited lower mechanical stability, while A146-F116, P135-F118, and A134-F118 were slightly weakened (Table S9 and Fig. S12).

In the JN.1 complex, two dissociation modes were observed. The dominant mode showed a single peak and was consistent with rigid-body dissociation, while a minority displayed partial unfolding of the Ab constant regions (Fig. 3A and B, and Fig. S12). The L chain detached first in all cases, followed by the H chain. When the L chain was pulled, unfolding occurred between Q200 and E216 before detachment. The L133-F118 contact was the most mechanically affected under either pulling condition, together with F175-S162, P176-V163, F175-T164, and A146-F116 for H-chain pulling, and P132-S121, F131-S121, F131-E123, and F131-Q124 for L-chain pulling.

3.3.2. S2X259/RBD complex. S2X259 is a broadly neutralizing Ab with exceptional affinity for the SARS-CoV-2 WT variant, (K_D < 0.1 nM).[31,35] It retains potent neutralizing activity across multiple variants of concern, including Omicron (K_D 1–86 nM), and also neutralized several zoonotic sarbecoviruses.[58,61] S2X259 recognizes a cryptic, structurally conserved RBD epitope (Y369–K386, G404–A411, and P499–Y508) that becomes accessible only in the open spike conformation. Although it does not directly contact the RBM, S2X259 sterically blocks hACE2 binding[58] (Table S9).

In the WT complex, pulling from the H chain mostly produced a single force peak (Fig. 2B). The RBD unfolded locally in residues P521–K529 before H-chain dissociation, followed by L-chain dissociation. In some trajectories, partial

unfolding of the H chain (N208–S226) occurred before dissociation, although the H chain still detached first. When pulling from the L chain, dissociation also began with RBD unfolding at A522-H530, often accompanied by limited L-chain unfolding between Q200-E216 (Fig. S1C and S13).

In the BA.4 complex, pulling from the H chain consistently led to RBD unfolding in A520–S529, after which the H chain dissociated first (Fig. S6). Most trajectories displayed rigid-body dissociation, though 10% exhibited unfolding within VH (V122–T146) or CH1 (H211–S226) prior to dissociation. Pulling from the L chain induced a stepwise unfolding, with sequential extension of residues Q200-E216 and L112-K135 before detachment (Fig. S5B). In these cases, the H chain remained bound, suggesting asymmetric force propagation through the complex. The JN.1 complex displayed the most heterogeneous mechanical response (Fig. 3B). When pulling from the H chain, some trajectories showed simultaneous detachment of both chains without significant unfolding, with local RBD deformation at L516–K528. Others showed limited H-chain unfolding (N210–S226) and sequential L-chain dissociation. Pulling from the L chain yielded either rigid-body dissociation or unfolding within T202-E216 before detachment (Fig. S6B).

Across variants, the RBD consistently unfolded near its C-terminal region (A516-S529) under force. Unfolding within the Ab was rare and confined to specific regions of VH (V122-T146, N208-226) and VL/CL (Q200-E216, D112-L135). These events were most pronounced in BA.4, whereas JN.1 exhibited reduced unfolding and more frequent rigid-body dissociation. These results indicate that S2X259 maintains high mechanical stability across variants, with a variant-specific redistribution of strain and slightly weaker inter-chain coupling in Omicron.

3.3.3. R1-32/RBD complex. R1-32 is a monoclonal Ab that targets a conserved a cryptic epitope located beneath the RBM of the SARS-CoV-2 RBD.[32] This site becomes fully accessible only when the RBD adopts the open conformation. Unlike hACE2-competing antibodies, R1-32 does not block receptor binding but instead promotes RBD opening and destabilizes the spike trimer, potentially driving it toward a non-functional state. In the WT complex, pulling from the H chain produced a characteristic sawtooth dissociation profile (Fig. 2C). The RBD consistently unfolded within residues S438–P507, while both Ab chains remained folded (Fig. S1E and F, S14 and Table S4). Dissociation proceeded sequentially: the L chain detached first, followed by disruption of constant-region contacts and eventual dissociation of the H chain. Pulling from the L chain yielded similar behavior, with identical RBD unfolding and chain detachment order. No unfolding was detected in either Ab chain. The reproducible unfolding of the S438-P507 segment coincided with mechanically labile regions previously identified in RBD pulling simulations β1 (A348-Y351) and β5 and β6 (V401, L452, Y451, Y453, R454, and L492)[49] (Fig. S15), whose disruption destabilizes the β-sheet core and propagates toward the RBM. The proximity of these clusters to S438-P507 explains its recurrent unfolding under force in the R1-32 complex.

In the BA.4 complex, pulling from the H chain resulted in sequential detachment: the L chain dissociated first, followed by unfolding of RBD residues (R454-P491) and then rigid-body dissociation of the Ab (Fig. S6C). No unfolding occurred in either chain. In 74% of the trajectories, RBD unfolding extended to residues S438–P507. The L chain produced similar results, with partial unfolding of the L-chain region V199-T213 preceding its dissociation (Fig. S6C, S2E and F, S14).

For the JN.1 complex, pulling from the H chain again produced RBD unfolding within S438–Y507, consistent with the WT response (Fig. 3C and Fig. S6C). The L chain detached first, followed by the H chain, with both remaining folded. Some trajectories exhibited more localized RBD deformation (R454–L491), but the overall sequence of events was conserved. Pulling from the L chain caused deformation of the RBD tip and loss of L–H inter-chain contacts, leading to complete L-chain dissociation, while the H chain remained bound and folded.

Altogether, R1-32 maintains a consistent, stepwise dissociation mechanism across variants. Force propagation leads to reproducible RBD unfolding within S438-P507, while the Ab remains structurally stable, highlighting its mechanically robust architecture.

3.3.4. Cooperative role of heavy (H) and light (L) chains under mechanical forces. To dissect the contribution of each chain to Ab mechanical stability, CG-SMD simulations were performed using single-chain systems (H-only or L-only) bound to the RBD in the WT background. In all cases, the maximum force (F_{max}) sustained by a single chain was lower than that of the two-chain Ab, underscoring the cooperative role of the H–L assembly. The complete complexes reached average F_{max} values of approximately 365 pN for PDI-231, 550 pN for S2X259, and 408 pN for R1-32 (Fig. 5). In comparison, H-only systems reached about 250 pN for PDI-231, 428 pN for S2X259, and 405 pN for R1-32, while L-only systems averaged around 200 pN. These results indicate that mechanical stability depends non-additively on both chains, with inter-chain coupling and asymmetric load distribution providing synergistic reinforcement.

For PDI-231, the complete complex reached about 365 pN, whereas isolated H and L chains withstood about 250 and 200 pN, respectively (Fig. 4A–C). The two-chain assembly delays dissociation and increases the rupture force beyond that of individual chains. In S2X259, the whole Ab complex exhibited the highest mechanical resistance (550 pN). The H chain carried most of the load (approximately 430 pN), consistent with the dominance of contacts at the H/RBD interface, while the L chain contributed peripheral stabilization and detached earlier. For R1-32, the total F_{max} (408 pN) was nearly identical to that of the isolated H chain (405 pN), indicating that mechanical force is transmitted almost exclusively through the H/RBD interface, with the L chain acting primarily as a stabilizing support.

Analysis of contact networks across all three Abs (Fig. 4D–F) confirmed that the majority of stabilizing contacts originate from the H chain, while the L chain contributes fewer contacts that enhance overall stability. This imbalance helps explain the dominance of the H chain in mechanical load transmission and the secondary stabilizing role of the L chain.

Across all systems, the L chain displayed a consistent mechanical response largely independent of epitope geometry,

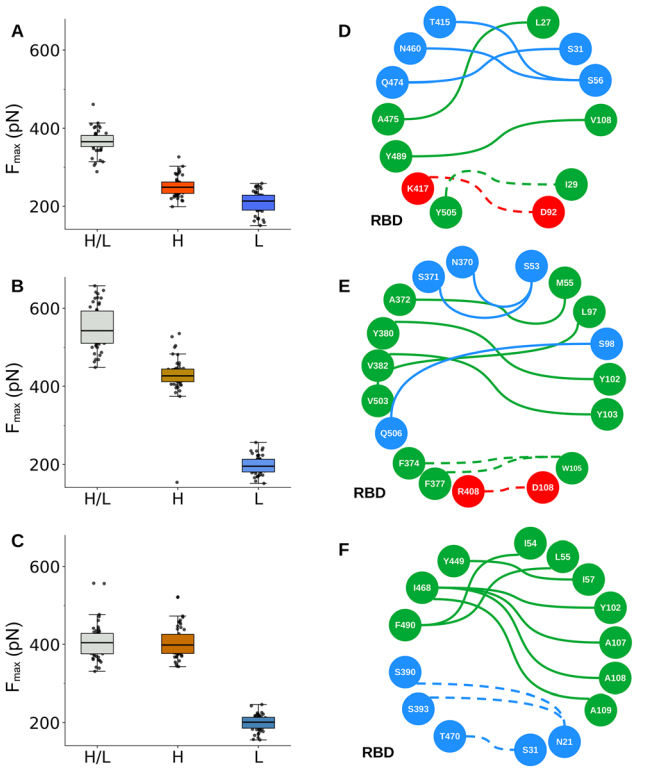

Fig. 4 Mechanical stability and interfacial networks of Ab/RBD WT complexes. (A–C) F_{max} values from CG-SMD simulations for PDI-231, S2X259, and R1-32, respectively. Boxplots compare the full Ab (H chain/L chain) with single-chain systems (H or L). Intact antibodies consistently sustain higher forces, reflecting cooperative stabilization between chains. (D–F) Network representation of chemistry-specific contacts within the Ab/RBD interfaces of PDI-231, S2X259, and R1-32, respectively. Solid and dashed lines indicate H chain/RBD and L chain/RBD contact pairs, respectively. Colors denote interaction type: red for ionic, blue for polar, and green for nonpolar. Amino acid nodes are colored according to chemical properties.

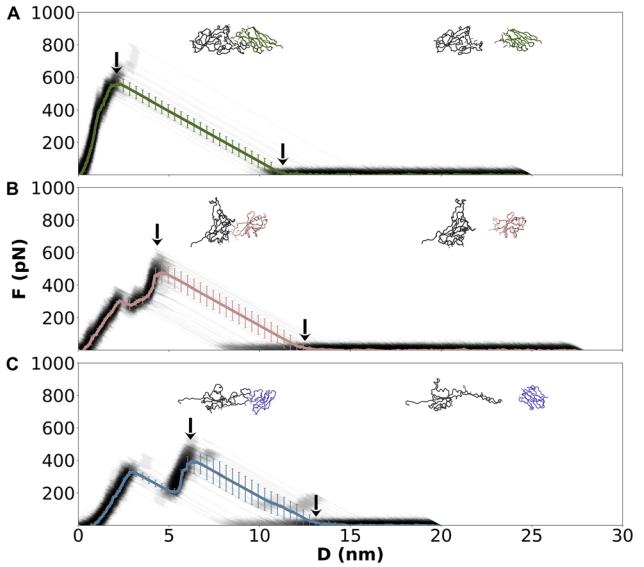

Fig. 5 Mechanical response of Nb/RBD WT complexes under constant-velocity pulling. Force–displacement profiles are shown for (A) R14, (B) C1, and (C) *n*3113.1 (gray traces, mean in color). Insets display representative structures at the maximum force (F_{max}, left arrow) and after dissociation (right arrow). Error bars denote standard deviations across 50 independent trajectories.

suggesting that it provides a baseline stabilizing function but cannot withstand large mechanical forces alone. The H chain, in contrast, serves as the principal conduit for force propagation through the RBD interface. Although each chain is individually less efficient, their combination creates an asymmetric yet cooperative mechanical architecture. This dual-chain organization amplifies force resistance through complementary roles: the H chain transmits load, while the L chain reinforces inter-chain stability. Such mechanical synergy likely reflects evolutionary optimization of Ab architecture for both structural robustness and adaptability.[62]

3.4. Nanomechanics of Nb/RBD complexes

The binding affinity and neutralization potency of Nbs have been extensively characterized, with several studies reporting high stability and strong neutralization across SARS-CoV-2 variants.[63,64] However, their mechanical behavior during force-induced dissociation remains largely unexplored to date.[15] In Nbs, the absence of an L chain simplifies the architecture but also raises the question of whether their compact design transmits force more directly to the RBD interface, potentially altering the dissociation pathway compared with Abs.

3.4.1. R14/RBD complex. The R14 Nb targets the RBM and engages the antigen through its three CDRs 1–3.[33] Similar to PDI-231, R14 can only bind the RBD in the up conformation. It exhibits ultrahigh affinity, with no detectable dissociation for the WT, Alpha, Kappa, and Delta variants, while its neutralization potency decreases against Omicron, with K_D values ranging from 0.57 nM to 43 nM.[33]

Mechanical dissociation of the RBD/R14 complex (PDB ID: 7WD1) was analyzed for the WT, BA.4, and JN.1 variants. In all cases, dissociation followed a rigid-body mechanism, with neither the Nb nor the RBD undergoing significant unfolding (Fig. 5A and Table S5). This consistent detachment mode indicates a stable and cooperative interface across variants.

Despite the shared mechanism, clear differences in F_{max} were observed (Table S11). The WT complex exhibited an average F_{max} of 596 ± 56 pN, reflecting high mechanical stability. The BA.4 complex reached an even higher F_{max} (648.6 ± 44 pN; Fig. S9A), suggesting enhanced resistance to mechanical stress, likely due to local reinforcement or reorganization of interfacial contacts introduced by BA.4-specific mutations (Tables S1 and S5). In contrast, JN.1 showed a pronounced decrease in F_{max} (346 ± 35 pN; Fig. 6A), indicating a loss of key stabilizing interactions and premature rupture under force.

3.4.2. C1/RBD complex. The C1 Nb binds the SARS-CoV-2 RBD with high affinity binding for WT, Alpha, and Beta variants, exhibiting K_D values in the 615–725 pM range.[34] Although C1 does not directly occlude the hACE2 binding site, it neutralizes the virus through steric hindrance by occupying

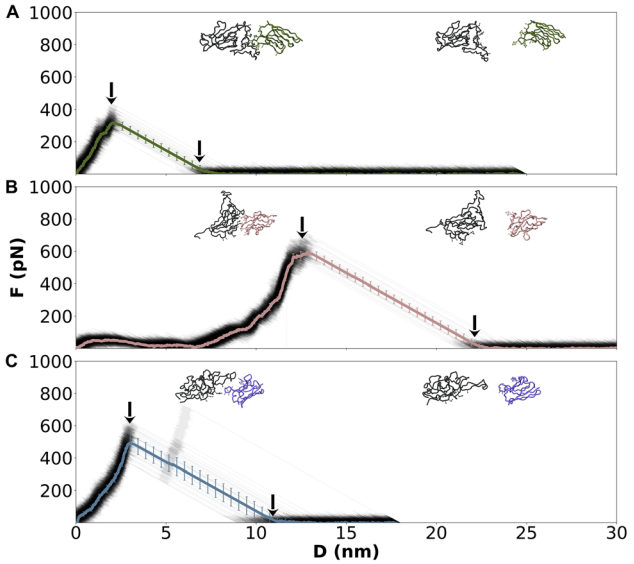

Fig. 6 Mechanical response of Nb/RBD JN.1 complexes under constant-velocity pulling. Same as Fig. 5.

spatially adjacent regions (see Fig. 1). The C1 epitope partially overlaps with that of S2X259, and its binding has been associated with spike destabilization, likely impairing receptor engagement by perturbing the structural organization of the RBD.[34]

In the WT system, all trajectories displayed a single prominent dissociation peak with an average F_{max} of 479 ± 89 pN, typically preceded by a brief drop in the mechanical force (Fig. 5B). The RBD unfolded between residues A520 and S530, distant from the RBM region, while dissociation proceeded *via* a rigid-body mechanism. The CDR3 loop was consistently the last element to disengage, consistent with its deep insertion into the epitope pocket (Table S6).

In the BA.4 complex, the mechanical response was more heterogeneous. Most CG-SMD trajectories exhibited a single force peak with an F_{max} of 513 ± 62 pN, preceded by a minor force drop similar to the WT (Fig. 5B and Fig. S9B). These cases involved partial unfolding of RBD residues F515–K528 followed by rigid-body dissociation. However, in approx. 30% of the trajectories, dissociation occurred without any detectable unfolding of either the RBD or the Nb, suggesting that BA.4 permits a direct rupture pathway in which interfacial contacts break without prior structural rearrangement.

For the JN.1 system, dissociation curves also exhibited a single sharp rupture event, with an average F_{max} of 603 ± 56. (Fig. 6B). The gradual buildup and convergence of the force profiles suggest a slightly more flexible interface compared with WT and BA.4, likely reflecting reduced contact density or altered packing geometry in JN.1. Dissociation remained rigid-body in character, with RBD unfolding limited to residues A520–S530 and no detectable deformation in the Nb. Collectively, the C1/RBD complexes exhibit robust mechanical stability across variants, maintaining a consistently rigid mechanism. Variant-dependent modulation of rupture forces reflects subtle alterations in interfacial packing and contact geometry rather than changes in the overall mechanical pathway.

3.4.3. *n*3113.1/RBD complex. The mechanical dissociation of the RBD–*n*3113.1 complex was analyzed for the WT, BA.4, and JN.1 variants. In the WT system, dissociation profiles displayed a complex sawtooth pattern reflecting sequential unfolding events in the RBD (Fig. 5C). Most trajectories showed two main unfolding regions: a partial loss of structure at the C-terminal segment (L517–K528) followed by broader unfolding in N437–P507 (Table S7). Despite these deformations, the Nb remained folded and dissociated as a rigid body. In a subset of seven trajectories, a single-force peak was observed, accompanied only by minor unfolding of the RBD C-terminus (L517–K528), again consistent with rigid-body detachment of *n*3113.1.

For the BA.4 complex, dissociation followed a predominantly single-peak profile characteristic of rigid-body rupture. In most simulations, both the RBD and Nb remained folded throughout the pulling process (Fig. S9C). Occasional small force bumps preceding the main rupture peak corresponded to slight unfolding of RBD residues L517–K528, but these events did not modify the overall dissociation mechanism. The JN.1 complex exhibited the simplest mechanical response (Fig. 6C). Most trajectories displayed a single, sharp rupture peak, without noticeable unfolding of either the RBD or the NB. In a few cases, limited unfolding of the RBD C-terminal residues L517–K528 preceded dissociation, but *n*3113.1 consistently maintained its structural integrity during dissociation. Overall, the RBD/n.3113.1 complexes exhibit robust mechanical stability across variants, dominated by rigid-body dissociation with minimal RBD deformation. The conserved unfolding of the L517-K528 region represents a local structural response to mechanical stress rather than a variant-specific alteration of the dissociation mechanism.

4. Conclusions

This study demonstrates how a structure-based CG approach built on the Martini 3 force field[26] can be extended to describe large protein conformational changes and mechanical responses in multidomain complexes. By optimizing native contacts through AA simulations, our implementation of GōMartini 3 achieves improved accuracy in capturing both equilibrium stability and mechanical unfolding pathways.[15,51] Although GōMartini 3 relies on a well-defined reference structure to parameterize secondary structure, this requirement provides a controlled framework for analyzing the mechanical limits of folded assemblies, complementing other CG models such as OLIVES, SIRAH, and UNRES, which have not yet been benchmarked under force. Recent methodological advances further extend GōMartini 3 to multimeric systems, enabling its application to diverse protein–protein assemblies beyond viral antigens.[65]

From a biological perspective, our results reveal how the mechanical behavior of SARS-CoV-2 RBD complexes reflects their molecular architecture and binding mode. In Abs, the dual-chain organization turned out to be inherently asymmetric

yet cooperative. The H chain acts as the principal conduit for force transmission, while the L chain stabilizes the complex through inter-chain reinforcement. This division of labor increases the rupture force beyond what either chain can sustain alone, emphasizing that mechanical resilience is an emergent property of the full antibody scaffold rather than a sum of individual components. Mutational effects were also found to shape mechanical outcomes: for example, the JN.1 variant exhibited more synchronous chain detachment and reduced unfolding, suggesting altered inter/domain coordination and rigidity.

Nb, in contrast, displayed simpler and more uniform mechanical profiles. Their compact, single-domain geometry allowed efficient transmission of force through a rigid interface, maintaining structural integrity even under high loads. Among the Nb systems, R14 achieved the highest rupture forces, particularly in the BA.4 variant. These results highlight that molecular size and architecture dictate how mechanical load is absorbed, distributed, or resisted at the interface.

Non-hACE2-competing complexes, such as R1-32 and *n*3113.1, revealed a different aspect of the RBD's mechanical landscape. In these systems, dissociation was consistently coupled to the unfolding of the S438–P507 region, a structurally labile β-sheet–loop–β-sheet motif identified in prior pulling experiments as a primary rupture hotspot. This recurring deformation suggests that certain RBD segments function as mechanical hinges that determine how force propagates through the domain. Variants modulate this behavior: BA.4 tends to strengthen interfacial networks, while JN.1 weakens them, indicating that viral evolution can tune mechanical resistance as an additional layer of functional adaptation.

Beyond explaining these variant-specific differences, the study provides design-oriented insights. First, antibodies and nanobodies that promote rigid-body detachment with high rupture forces are likely to retain binding under physiological mechanical stress, such as shear flow, receptor internalization, or immune-cell traction. Second, enhancing hydrophobic and aromatic packing within the H-chain interface while maintaining inter-chain complementarity can improve mechanical endurance without compromising flexibility. Third, nanobody-based scaffolds may be ideal for targeting conserved, cryptic epitopes where compact geometry favors both access and force resilience.

Overall, this work positions mechanical resilience as a quantitative complement to affinity in evaluating therapeutic potential. Incorporating force-dependent stability into antibody or nanobody design offers a more complete description of how these molecules perform *in vivo*, where tensile and shear stresses influence viral adhesion, immune engagement, and drug efficacy. The same framework can be extended to other sarbecoviruses, for which high-resolution RBD structures and cross-neutralizing antibodies are available, and even to antibodies targeting mechanosensitive receptors in oncology, where cellular traction and matrix stiffness are critical determinants of therapeutic success.

By integrating molecular mechanics with structural bioinformatics, the GōMartini 3 methodology provides a scalable and predictive platform for exploring how proteins resist or yield under stress. This approach thus bridges physical modeling and therapeutic engineering, offering actionable guidelines for designing next-generation antibodies and nanobodies that couple biochemical affinity with mechanical robustness across viral and cellular systems.

Author contributions

L. F. C. V.: writing – review & editing, writing – original draft, methodology, investigation, formal analysis. G. E. O. R.: review, scientific discussion,. A. B. P.: writing – review & editing, writing – original draft, supervision, methodology, investigation, funding acquisition, conceptualization. S.-J. M.: writing – review & editing, scientific discussion.

Conflicts of interest

There are no conflicts to declare.

Data availability

The data supporting the findings of this study are openly available in the Zenodo repository: https://zenodo.org/records/15608522. The repository includes all input files and simulations utilized in this research.

Supplementary information (SI): all-atom molecular dynamics and coarse-grained steered MD simulations for the comparative nanomechanical analysis of antibodies and nanobodies bound to SARS-CoV-2 RBD variants. See DOI: https://doi.org/10.1039/d6cp00556j.

Acknowledgements

A. B. P. acknowledges financial support from the National Science Center, Poland, under grant 2022/45/B/NZ1/02519 and gratefully acknowledges Polish high-performance computing infrastructure PLGrid (HPC Center: ACK Cyfronet AGH) for providing computer facilities and support within computational grant no. PLG/2024/017332 and PLG/2025/018510.

References

1 W. Msemburi, A. Karlinsky, V. Knutson, S. Aleshin-Guendel, S. Chatterji and J. Wakefield, *Nature*, 2023, **613**, 130–137.
2 S. Zhou, P. Lv, M. Li, Z. Chen, H. Xin, S. Reilly and X. Zhang, *Biomed. Pharmacother.*, 2023, **159**, 114242.
3 A. Sternberg and C. Naujokat, *Life Sci.*, 2020, **257**, 118056.
4 J. Zhang, T. Xiao, Y. Cai and B. Chen, *Curr. Opin. Virol.*, 2021, **50**, 173–182.
5 J. Lan, J. Ge, J. Yu, S. Shan, H. Zhou, S. Fan, Q. Zhang, X. Shi, Q. Wang, L. Zhang and X. Wang, *Nature*, 2020, **581**, 215–220.
6 A. Deshpande, B. D. Harris, L. Martinez-Sobrido, J. J. Kobie and M. R. Walter, *Front. Immunol.*, 2021, **12**, 691715.
7 A. Ray, T. T. Minh Tran, R. D. Santos Natividade, R. A. Moreira, J. D. Simpson, D. Mohammed, M. Koehler, S. J. L.

Petitjean, Q. Zhang, F. Bureau, L. Gillet, A. B. Poma and D. Alsteens, *ACS Nanosci. Au*, 2024, **4**, 136–145.
8 G. E. Olivos-Ramirez, L. F. Cofas-Vargas, T. Madl and A. B. Poma, *Pathogens*, 2025, **14**, 274.
9 S. Kim, Y. Liu, M. Ziarnik, Y. Cao, X. F. Zhang and W. Im, *J. Comput. Chem.*, 2022, **44**(4), 594–601.
10 P. Han, L. Li, S. Liu, Q. Wang, D. Zhang, Z. Xu, P. Han, X. Li, Q. Peng, C. Su, B. Huang, D. Li, R. Zhang, M. Tian, L. Fu, Y. Gao, X. Zhao, K. Liu, J. Qi, G. F. Gao and P. Wang, *Cell*, 2022, **185**, 630–640.e10.
11 A. Mittal, K. Manjunath, R. K. Ranjan, S. Kaushik, S. Kumar and V. Verma, *PLoS Pathog.*, 2020, **16**, e1008762.
12 R. Yan, Y. Zhang, Y. Li, F. Ye, Y. Guo, L. Xia, X. Zhong, X. Chi and Q. Zhou, *Cell Res.*, 2021, **31**, 717–719.
13 D. Koirala, P. M. Yangyuoru and H. Mao, *Rev. Anal. Chem.*, 2013, **32**, 197–208.
14 W. Liu, D. Tang, X.-X. Xu, Y.-J. Liu and Y. Jiu, *Front. Bioeng. Biotechnol.*, 2021, **9**, 764516.
15 L. F. Cofas-Vargas, G. E. Olivos-Ramirez, M. Chwastyk, R. A. Moreira, J. L. Baker, S. J. Marrink and A. B. Poma, *Nanoscale*, 2024, **16**, 18824–18834.
16 M. Golcuk, A. Hacisuleyman, S. Z. Yilmaz, E. Taka, A. Yildiz and M. Gur, *J. Chem. Inf. Model.*, 2022, **62**, 2490–2498.
17 M. Golcuk, A. Hacisuleyman, B. Erman, A. Yildiz and M. Gur, *J. Chem. Inf. Model.*, 2021, **61**, 5152–5160.
18 H. Nguyen and M. S. Li, *Sci. Rep.*, 2022, **12**, 1–15.
19 S. Muyldermans and V. V. Smider, *Curr. Opin. Immunol.*, 2016, **40**, 7–13.
20 B.-K. Jin, S. Odongo, M. Radwanska and S. Magez, *Int. J. Mol. Sci.*, 2023, **24**, 5994.
21 J. Huo, A. Le Bas, R. R. Ruza, H. M. E. Duyvesteyn, H. Mikolajek, T. Malinauskas, T. K. Tan, P. Rijal, M. Dumoux, P. N. Ward, J. Ren, D. Zhou, P. J. Harrison, M. Weckener, D. K. Clare, V. K. Vogirala, J. Radecke, L. Moynié, Y. Zhao, J. Gilbert-Jaramillo, M. L. Knight, J. A. Tree, K. R. Buttigieg, N. Coombes, M. J. Elmore, M. W. Carroll, L. Carrique, P. N. M. Shah, W. James, A. R. Townsend, D. I. Stuart, R. J. Owens and J. H. Naismith, *Nat. Struct. Mol. Biol.*, 2020, **27**, 846–854.
22 D. K. Agarwal, V. Nandwana, S. E. Henrich, V. P. V. N. Josyula, C. S. Thaxton, C. Qi, L. M. Simons, J. F. Hultquist, E. A. Ozer, G. S. Shekhawat and V. P. Dravid, *Biosens. Bioelectron.*, 2022, **195**, 113647.
23 M. L. Tonkin and M. J. Boulanger, *PLoS Pathog.*, 2015, **11**, e1004539.
24 P. Saha, I. Fernandez, F. Sumbul, C. Valotteau, D. Kostrz, A. Meola, E. Baquero, A. Sharma, J. R. Portman, F. Stransky, T. Boudier, P. Guardado-Calvo, C. Gosse, T. Strick, F. A. Rey and F. Rico, *Nat. Nanotechnol.*, 2025, **20**, 926–934.
25 P. C. T. Souza, L. Borges-Araújo, C. Brasnett, R. A. Moreira, F. Grünewald, P. Park, L. Wang, H. Razmazma, A. C. Borges-Araújo, L. F. Cofas-Vargas, L. Monticelli, R. Mera-Adasme, M. N. Melo, S. Wu, S. J. Marrink, A. B. Poma and S. Thallmair, *Nat. Commun.*, 2025, **16**, 4051.
26 P. C. T. Souza, R. Alessandri, J. Barnoud, S. Thallmair, I. Faustino, F. Grünewald, I. Patmanidis, H. Abdizadeh, B. M. H. Bruininks, T. A. Wassenaar, P. C. Kroon, J. Melcr, V. Nieto, V. Corradi, H. M. Khan, J. Domański, M. Javanainen, H. Martinez-Seara, N. Reuter, R. B. Best, I. Vattulainen, L. Monticelli, X. Periole, D. P. Tieleman, A. H. de Vries and S. J. Marrink, *Nat. Methods*, 2021, **18**, 382–388.
27 A. B. Poma, M. Cieplak and P. E. Theodorakis, *J. Chem. Theory Comput.*, 2017, **13**, 1366–1374.
28 K. Wołek, À. Gómez-Sicilia and M. Cieplak, *J. Chem. Phys.*, 2015, **143**, 243105.
29 L. F. Cofas-Vargas, P. Mendoza-Espinosa, F. D. Montalvo-Sandoval, S. Pérez-Rodríguez, J. A. Rauda-Ceja, P. Hernández-Peralta, A. Durán-Vargas, M. A. Trujillo-Roldán, N. A. Valdez-Cruz and E. García-Hernández, *MAbs*, 2025, **17**, 2575083.
30 A. K. Wheatley, P. Pymm, R. Esterbauer, M. H. Dietrich, W. S. Lee, D. Drew, H. G. Kelly, L.-J. Chan, F. L. Mordant, K. A. Black, A. Adair, H.-X. Tan, J. A. Juno, K. M. Wragg, T. Amarasena, E. Lopez, K. J. Selva, E. R. Haycroft, J. P. Cooney, H. Venugopal, L. L. Tan, M. T. O. Neill, C. C. Allison, D. Cromer, M. P. Davenport, R. A. Bowen, A. W. Chung, M. Pellegrini, M. T. Liddament, A. Glukhova, K. Subbarao, S. J. Kent and W.-H. Tham, *Cell Rep.*, 2021, **37**, 109822.
31 T. N. Starr, N. Czudnochowski, Z. Liu, F. Zatta, Y.-J. Park, A. Addetia, D. Pinto, M. Beltramello, P. Hernandez, A. J. Greaney, R. Marzi, W. G. Glass, I. Zhang, A. S. Dingens, J. E. Bowen, M. A. Tortorici, A. C. Walls, J. A. Wojcechowskyj, A. De Marco, L. E. Rosen, J. Zhou, M. Montiel-Ruiz, H. Kaiser, J. R. Dillen, H. Tucker, J. Bassi, C. Silacci-Fregni, M. P. Housley, J. di Iulio, G. Lombardo, M. Agostini, N. Sprugasci, K. Culap, S. Jaconi, M. Meury, E. Dellota Jr, R. Abdelnabi, S.-Y. C. Foo, E. Cameroni, S. Stumpf, T. I. Croll, J. C. Nix, C. Havenar-Daughton, L. Piccoli, F. Benigni, J. Neyts, A. Telenti, F. A. Lempp, M. S. Pizzuto, J. D. Chodera, C. M. Hebner, H. W. Virgin, S. P. J. Whelan, D. Veesler, D. Corti, J. D. Bloom and G. Snell, *Nature*, 2021, **597**, 97–102.
32 P. He, B. Liu, X. Gao, Q. Yan, R. Pei, J. Sun, Q. Chen, R. Hou, Z. Li, Y. Zhang, J. Zhao, H. Sun, B. Feng, Q. Wang, H. Yi, P. Hu, P. Li, Y. Zhang, Z. Chen, X. Niu, X. Zhong, L. Jin, X. Liu, K. Qu, K. A. Ciazynska, A. P. Carter, J. A. G. Briggs, J. Chen, J. Liu, X. Chen, J. He, L. Chen and X. Xiong, *Nat. Microbiol.*, 2022, **7**, 1635–1649.
33 H. Liu, L. Wu, B. Liu, K. Xu, W. Lei, J. Deng, X. Rong, P. Du, L. Wang, D. Wang, X. Zhang, C. Su, Y. Bi, H. Chen, W. J. Liu, J. Qi, Q. Cui, S. Qi, R. Fan, J. Jiang, G. Wu, G. F. Gao and Q. Wang, *Cell Rep. Med.*, 2023, **4**, 100918.
34 J. Huo, H. Mikolajek, A. Le Bas, J. J. Clark, P. Sharma, A. Kipar, J. Dormon, C. Norman, M. Weckener, D. K. Clare, P. J. Harrison, J. A. Tree, K. R. Buttigieg, F. J. Salguero, R. Watson, D. Knott, O. Carnell, D. Ngabo, M. J. Elmore, S. Fotheringham, A. Harding, L. Moynié, P. N. Ward, M. Dumoux, T. Prince, Y. Hall, J. A. Hiscox, A. Owen, W. James, M. W. Carroll, J. P. Stewart, J. H. Naismith and R. J. Owens, *Nat. Commun.*, 2021, **12**, 5469.
35 Z. Yang, Y. Wang, Y. Jin, Y. Zhu, Y. Wu, C. Li, Y. Kong, W. Song, X. Tian, W. Zhan, A. Huang, S. Zhou, S. Xia, X. Tian, C. Peng, C. Chen, Y. Shi, G. Hu, S. Du, Y. Wang,

Y. Xie, S. Jiang, L. Lu, L. Sun, Y. Song and T. Ying, *Signal Transduction Targeted Ther.*, 2021, **6**, 378.
36 A. Sali and T. L. Blundell, *J. Mol. Biol.*, 1993, **234**, 779–815.
37 C. Tian, K. Kasavajhala, K. A. A. Belfon, L. Raguette, H. Huang, A. N. Migues, J. Bickel, Y. Wang, J. Pincay, Q. Wu and C. Simmerling, *J. Chem. Theory Comput.*, 2020, **16**, 528–552.
38 D. A. Case, H. M. Aktulga, K. Belfon, I. Y. Ben-Shalom, J. T. Berryman, S. R. Brozell, D. S. Cerutti, T. E. Cheatham III, G. A. Cisneros, V. W. D. Cruzeiro, T. A. Darden, N. Forouzesh, M. Ghazimirsaeed, G. Giambaşu, T. Giese, M. K. Gilson, H. Gohlke, A. W. Goetz, J. Harris, Z. Huang, S. Izadi, S. A. Izmailov, K. Kasavajhala, M. C. Kaymak, A. Kovalenko, T. Kurtzman, T. S. Lee, P. Li, Z. Li, C. Lin, J. Liu, T. Luchko, R. Luo, M. Machado, M. Manathunga, K. M. Merz, Y. Miao, O. Mikhailovskii, G. Monard, H. Nguyen, K. A. O'Hearn, A. Onufriev, F. Pan, S. Pantano, A. Rahnamoun, D. R. Roe, A. Roitberg, C. Sagui, S. Schott-Verdugo, A. Shajan, J. Shen, C. L. Simmerling, N. R. Skrynnikov, J. Smith, J. Swails, R. C. Walker, J. Wang, J. Wang, X. Wu, Y. Wu, Y. Xiong, Y. Xue, D. M. York, C. Zhao, Q. Zhu and A. P. Kollman, 2024, Amber, University of California and S. Francisco., *Amber24*, 2024, DOI: 10.1021/acs.jcim.5c01063.
39 R. Salomon-Ferrer, A. W. Götz, D. Poole, S. Le Grand and R. C. Walker, *J. Chem. Theory Comput.*, 2013, **9**, 3878–3888.
40 P. Eastman, J. Swails, J. D. Chodera, R. T. McGibbon, Y. Zhao, K. A. Beauchamp, L.-P. Wang, A. C. Simmonett, M. P. Harrigan, C. D. Stern, R. P. Wiewiora, B. R. Brooks and V. S. Pande, *PLoS Comput. Biol.*, 2017, **13**, e1005659.
41 S. Izadi, R. Anandakrishnan and A. V. Onufriev, *J. Phys. Chem. Lett.*, 2014, **5**, 3863–3871.
42 A. C. Simmonett and B. R. Brooks, *J. Chem. Phys.*, 2021, **154**, 054112.
43 D. S. Cerutti, R. E. Duke, T. A. Darden and T. P. Lybrand, *J. Chem. Theory Comput.*, 2009, **5**, 2322.
44 D. J. Sindhikara, S. Kim, A. F. Voter and A. E. Roitberg, *J. Chem. Theory Comput.*, 2009, **5**, 1624–1631.
45 J. Åqvist, P. Wennerström, M. Nervall, S. Bjelic and B. O. Brandsdal, *Chem. Phys. Lett.*, 2004, **384**, 288–294.
46 J.-P. Ryckaert, G. Ciccotti and H. J. C. Berendsen, *J. Comput. Phys.*, 1977, **23**, 327–341.
47 M. R. Shirts, C. Klein, J. M. Swails, J. Yin, M. K. Gilson, D. L. Mobley, D. A. Case and E. D. Zhong, *J. Comput. Aided Mol. Des.*, 2017, **31**, 147–161.
48 C. W. Hopkins, S. Le Grand, R. C. Walker and A. E. Roitberg, *J. Chem. Theory Comput.*, 2015, **11**, 1864–1874.
49 R. A. Moreira, M. Chwastyk, J. L. Baker, H. V. Guzman and A. B. Poma, *Nanoscale*, 2020, **12**, 16409–16413.
50 A. B. Poma, T. T. M. Thu, L. T. M. Tri, H. L. Nguyen and M. S. Li, *J. Phys. Chem. B*, 2021, **125**, 7628–7637.
51 Z. Liu, R. A. Moreira, A. Dujmović, H. Liu, B. Yang, A. B. Poma and M. A. Nash, *Nano Lett.*, 2022, **22**, 179–187.
52 P. C. Kroon, F. Grunewald, J. Barnoud, M. van Tilburg, P. C. T. Souza, T. A. Wassenaar and S. J. Marrink, *eLife*, 2025, **12**, RP90627.
53 R. P. Joosten, T. A. H. te Beek, E. Krieger, M. L. Hekkelman, R. W. W. Hooft, R. Schneider, C. Sander and G. Vriend, *Nucleic Acids Res.*, 2011, **39**, D411–9.
54 L. F. Cofas-Vargas, R. A. Moreira, S. Poblete, M. Chwastyk and A. B. Poma, *Acta Phys. Pol., A*, 2024, **145**, S9–S9.
55 G. Bussi, D. Donadio and M. Parrinello, *J. Chem. Phys.*, 2007, **126**, 014101.
56 M. Bernetti and G. Bussi, *J. Chem. Phys.*, 2020, **153**, 114107.
57 M. J. Abraham, T. Murtola, R. Schulz, S. Páll, J. C. Smith, B. Hess and E. Lindahl, *SoftwareX*, 2015, **1–2**, 19–25.
58 M. A. Tortorici, N. Czudnochowski, T. N. Starr, R. Marzi, A. C. Walls, F. Zatta, J. E. Bowen, S. Jaconi, J. Di Iulio, Z. Wang, A. De Marco, S. K. Zepeda, D. Pinto, Z. Liu, M. Beltramello, I. Bartha, M. P. Housley, F. A. Lempp, L. E. Rosen, E. Dellota Jr, H. Kaiser, M. Montiel-Ruiz, J. Zhou, A. Addetia, B. Guarino, K. Culap, N. Sprugasci, C. Saliba, E. Vetti, I. Giacchetto-Sasselli, C. S. Fregni, R. Abdelnabi, S.-Y. C. Foo, C. Havenar-Daughton, M. A. Schmid, F. Benigni, E. Cameroni, J. Neyts, A. Telenti, H. W. Virgin, S. P. J. Whelan, G. Snell, J. D. Bloom, D. Corti, D. Veesler and M. S. Pizzuto, *Nature*, 2021, **597**, 103–108.
59 Q. He, L. Wu, Z. Xu, X. Wang, Y. Xie, Y. Chai, A. Zheng, J. Zhou, S. Qiao, M. Huang, G. Shang, X. Zhao, Y. Feng, J. Qi, G. F. Gao and Q. Wang, *Cell Rep. Med.*, 2023, **4**, 100991.
60 H. Ma, C. Ó'Fágáin and R. O'Kennedy, *Biochimie*, 2020, **177**, 213–225.
61 M. Li, F. Lou and H. Fan, *Signal Transduction Targeted Ther.*, 2022, **7**, 28.
62 P. Dudzic, D. Chomicz, W. Bielska, I. Jaszczyszyn, M. Zieliński, B. Janusz, S. Wróbel, M.-M. Le Pannérer, A. Philips, P. Ponraj, S. Kumar and K. Krawczyk, *Commun. Biol.*, 2025, **8**, 1110.
63 D. Wrapp, D. De Vlieger, K. S. Corbett, G. M. Torres, N. Wang, W. Van Breedam, K. Roose, L. van Schie, VIB-CMB COVID-19 Response Team, M. Hoffmann, S. Pöhlmann, B. S. Graham, N. Callewaert, B. Schepens, X. Saelens and J. S. McLellan, *Cell*, 2020, **181**, 1004–1015.e15.
64 Y. Xiang, S. Nambulli, Z. Xiao, H. Liu, Z. Sang, W. P. Duprex, D. Schneidman-Duhovny, C. Zhang and Y. Shi, *Science*, 2020, **370**, 1479–1484.
65 K. Korshunova, J. Kiuru, J. Liekkinen, G. Enkavi, I. Vattulainen and B. M. H. Bruininks, *J. Chem. Theory Comput.*, 2024, **20**, 7635–7645.